The Current Density Distribution in a Segmented-in-Series SOFC

B. A. Haberman
e-mail: b.haberman.01@cantab.net

A. J. Marquis
e-mail: a.marquis@imperial.ac.uk

The Department of Mechanical Engineering,
Imperial College London,
Exhibition Road,
South Kensington,
London SW7 2AZ, UK

A common tubular solid oxide fuel cell (SOFC) design consists of segmented-in-series electrochemical cells fabricated onto the outside of a porous support tube. Predicting the performance of this type of SOFC requires a detailed understanding of the current density distribution within each cell. This distribution is strongly coupled to the activation, concentration, and Ohmic losses, which occur as a result of the physical transport processes within the cell. A new computer code, known as the SOHAB code, has been developed to simulate these physical processes and thus make predictions of cell performance. The simulation results show how the magnitude of each loss varies spatially within the cell, causing the calculated current density distribution to be very different from that predicted by the established purely Ohmic models. At low currents the cell behavior is dominated by activation losses producing a very flat distribution. At moderate currents the Ohmic losses become more important, and the distribution is peaked at the edges of the electrolyte. At high currents the increased concentration losses flatten the distribution in the middle of the cell but not near its edges where gases flow from the surrounding inactive regions and the losses remain small. At low and moderate currents, the calculated current density distribution is sufficiently flat that the assumption of a uniform distribution can be used in conjunction with a one-dimensional model. However, at high currents this simplified model overestimates the concentration loss as it cannot account for the improved mass transport near the electrolyte edges. [DOI: 10.1115/1.2971047]

1 Introduction

The solid oxide fuel cell (SOFC) generates electrical power very efficiently from the direct electrochemical oxidation of fuel. In general, this type of fuel cell is made up of three very thin ceramic layers, with a porous electrode on either side of a solid oxide electrolyte. Structural strength is often provided by printing the cells directly onto a porous support layer, and it is common to print a row of segmented-in-series cells rather than one large continuous cell. This paper is concerned with simulating the physical transport processes within such a fuel cell and predicting how the current density distribution and cell performance are affected by the spatial variation of the internal loss mechanisms.

1.1 Background. The SOFC generates electrical power directly from the oxidation of hydrogen,

$$H_2 + \tfrac{1}{2}O_2 \rightarrow H_2O(\Delta \bar{G}^o_{298} = 228.6 \text{ kJ mol}^{-1}) \tag{1}$$

To a lesser extent, carbon monoxide is also oxidized by an electrochemical reaction [1], but this contribution will be ignored. The fuel and oxidant are separated by a semipermeable solid oxide electrolyte, and the half-cell reactions

$$\tfrac{1}{2}O_2 + 2e^- \rightarrow O^{2-} \tag{2}$$

$$H_2 + O^{2-} \rightarrow H_2O + 2e^- \tag{3}$$

occur at its interfaces with the porous cathode and anode (see Fig. 1). On open circuit, the fuel cell operates reversibly, and its output voltage is given in terms of the gas conditions on the outer surfaces of the cell by the Nernst potential $E_{N,\text{cell}}$,

$$E_{N,\text{cell}} = -\frac{[\Delta \bar{G}^o_T]}{n_e F} + \frac{\bar{R}T}{n_e F} \ln\left(\frac{p_{H_2} p^{1/2}_{O_2}}{p_{H_2O} p^{o\,1/2}}\right) \tag{4}$$

where $\Delta \bar{G}^o_T$ is the molar Gibbs function change for the overall reaction (1) at temperature T and standard pressure p^o, p_n is the partial pressure of gas species n, F is Faraday's constant, $\bar{R}$ is the universal gas constant, and n_e is the number of electrons released per molecule of hydrogen oxidized. When a current is drawn, E_{cell} is reduced from the ideal value $E_{N,\text{cell}}$ by the concentration loss ΔE_C, which arises because of mass transport within the porous components, the activation loss ΔE_A, which occurs as a result of the electrochemical reaction kinetics, and the Ohmic loss ΔE_R, which is the voltage drop caused by the current flow within the cell. Hence E_{cell} is given by

$$E_{\text{cell}} = E_{N,\text{cell}} - \Delta E_C - \Delta E_A - \Delta E_R \tag{5}$$

The derivation of Eq. (4) and further details of SOFC system design can be found in Ref. [2].

1.2 Segmented-in-Series SOFCs. In order to minimize the losses within a SOFC, very thin cell components are often used ($\leqslant 50\ \mu$m), and in some cases physical strength is provided by fabricating the cells on a tubular supporting structure. The surface area available on the outside of each tube is often subdivided into a row of cells, which are connected in series, a design commonly referred to as "segmented-in-series." There are several designs of this type currently being developed [3–6], and a typical configuration based on the Rolls-Royce Fuel Cell Systems Ltd. integrated planar-solid oxide fuel cell (IP-SOFC) design [3] is shown in Fig.

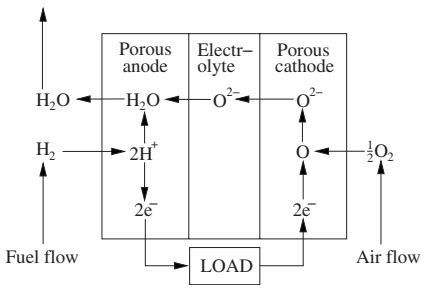

Fig. 1 Gas and ion transport and electrochemical reactions in a SOFC

Manuscript received March 17, 2007; final manuscript received March 18, 2008; published online February 23, 2009. Review conducted by Nigel M. Sammes.

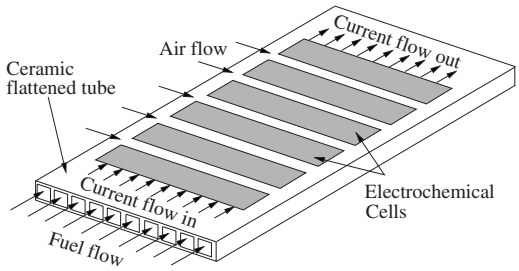

Fig. 2 The Rolls Royce Fuel Cell Systems Ltd. IP-SOFC

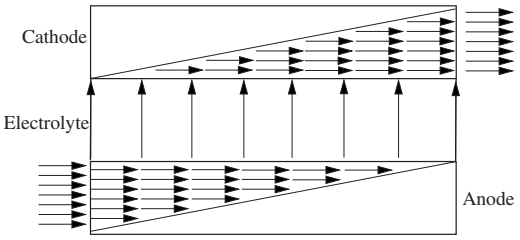

Fig. 4 Conventional current flow path analyzed in Refs. [7,8]

2. The porous cathode is the outermost layer of each cell and is supplied with oxygen from the air flowing over the outside of the tube, and the porous anode is printed directly onto the tube surface and is supplied with reformed fuel from the internal gas channels. The parts of the outer tube surface not covered by fuel cells are sealed with a glass layer.

Figure 3 shows a cross-section through the fuel cell layers, with arrows indicating the direction of conventional current flow. In this design of fuel cell, the net current flow is in the horizontal direction, and the current produced by each cell is collected by the electrodes. An analytical solution exists for the current flow in this cell geometry [7,8], which assumes that it flows unidirectionally in each layer (see Fig. 4). However, this approach is limited to analyzing the current flow through an arrangement of conductors because no account can be taken of the interaction between the current flow field and the cell losses ΔE_C and ΔE_A. Lai and Barnett [9] simulated the current flow in a segmented-in-series cell numerically but did not include the effects of these losses in their work. Several numerical studies included these effects, but they were focused on other types of SOFC [10–13]. Haberman and Young [14] made an initial attempt to include the cell losses in a segmented-in-series current flow simulation and reported significantly different current density distributions from previous work [7–9].

This paper is concerned with predicting the performance and current density distribution of the segmented-in-series cell shown in Fig. 3 using a steady-state simulation of the current flow field. The interaction between the cell irreversibilities and the current flow field is included by simulating the mass transport within the porous layers and the kinetics of the electrochemical reactions.

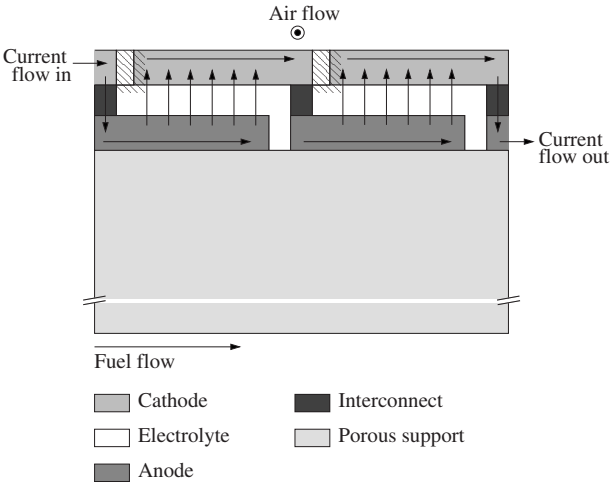

Fig. 3 Cross-section through a row of segmented-in-series cells

2 Key Physical Processes

Several key physical processes must be modeled in order to make accurate predictions of the current flow field.

2.1 Mass Transport in Porous Materials. Gas transport within a porous material depends on the Knudsen number Kn, defined by $\mathrm{Kn}=\lambda/d_p$, where λ is a length scale of the order of a molecular mean free path and d_p is a mean pore diameter. Young and Todd [15] derived the cylindrical pore interpolation model (CPIM), which provides a rigorous basis for describing multicomponent flow along a cylindrical pore of an arbitrary size. The CPIM can correctly predict both variations in gas mixture composition and pressure along a cylindrical pore. This model has been used to analyze the behavior of the IP-SOFC porous materials [16] and is also used in this study.

Conventionally, the total mass flux vector $\mathbf{G}_n$ of gas species n in a mixture of N gases can be decomposed into the sum of its convection and diffusion components,

$$\mathbf{G}_n = Y_n \mathbf{G} + \mathbf{G}_n^d \tag{6}$$

where Y_n is the mass fraction of species n, $\mathbf{G}$ is the total or convective mass flux vector of the mixture, and $\mathbf{G}_n^d$ is the diffusion flux vector of species n. $\mathbf{G}$ is defined by

$$\mathbf{G} = \sum_{k=1}^{N} \mathbf{G}_k \tag{7}$$

and hence $\mathbf{G}_n^d$ can be found from $\mathbf{G}_n$ and Eqs. (6) and (7).

For a mixture of N gases, the CPIM consists of a set of N equations written in terms of the total species flux vectors $\mathbf{G}_n$ per unit cross-sectional area of porous materials. There is a set of $N-1$ independent Stefan–Maxwell relations

$$\frac{\varepsilon}{\beta^2} \nabla X_n = \frac{\tilde{M}}{\rho_g} \sum_{n=1}^{N} \left[\frac{\mathbf{G}_m X_n}{M_m D_{mn}^e} - \frac{\mathbf{G}_n X_m}{M_n D_{nm}^e} \right] \tag{8}$$

and one pressure gradient equation

$$\frac{\varepsilon}{\beta^2} \nabla p = -A \sum_{n=1}^{N} \mathbf{G}_n / \sqrt{M_n} \tag{9}$$

where ε is the material porosity, β is its tortuosity, $\tilde{M}$ is the mean molar mass of the gas mixture, and X_n and M_n are the mole fraction and molar mass of species n. D_{nm}^e, D_{mn}^e, and A are interpolated coefficients, which are given by

$$\frac{1}{D_{nm}^e} = \frac{1}{D_{nm}} + \frac{1}{D_{k,n}}$$

$$\frac{1}{D_{mn}^e} = \frac{1}{D_{mn}} + \frac{1}{D_{k,m}} \tag{10}$$

$$\frac{1}{A} = \frac{1}{A^0} + \frac{1}{A^\infty} \tag{11}$$

where $D_{nm}=D_{mn}$ are binary (continuum) diffusion coefficients. $D_{k,n}$ is a free molecule or Knudsen term for species n and is given by

$$D_{k,n} = \frac{d_p}{3}\bar{\omega}_n \tag{12}$$

where $\bar{\omega}_n$ is the mean molecular speed of gas species n and $\overline{\omega_n} = \sqrt{(8\bar{R}T/\pi M_n)}$. A^0 and A^∞ are the continuum and free molecule pressure terms, respectively, which are given by

$$A^0 = \frac{32\tilde{\mu}_g}{\rho_g d_p^2 \sum_{n=1}^{N} Y_n/\sqrt{M_n}} \tag{13}$$

$$A^\infty = \frac{3}{d_p}\left(\frac{\bar{R}T\pi}{8}\right)^{1/2} \tag{14}$$

where $\tilde{\mu}_g$ and ρ_g are the dynamic viscosity and density of the gas mixture. Further details of the CPIM and its derivation (including a discussion of the phenomenon of "diffusion-slip," which has a strong effect on the solid wall boundary condition) are given in Young and Todd [15].

2.2 Current Flow. The flow of electric or ionic current within a conductor is modeled using the basic Ohm's law expression

$$\mathbf{i} = -\sigma \nabla \phi \tag{15}$$

where σ is the electrical or ionic conductivity of the material, ϕ is the electric field potential, and $\mathbf{i}$ is the current density vector.

2.3 Electrochemistry. In this study, mass transport in the porous layers and the current flow are simulated numerically, and hence the concentration and Ohmic losses are automatically accounted for. Therefore, the kinetics of the half-cell reactions (Eqs. (2) and (3)) are modeled based on the calculated local gas conditions at the cathode/electrolyte interface (CEI) and anode/electrolyte interface (AEI). At equilibrium the potential difference across a point on the CEI is given by

$$\phi_c - \phi_e = E_{N,c} = -\frac{[\Delta\overline{G}_{cT}^{o}]}{n_e F} + \frac{\bar{R}T}{n_e F}\ln\left(\frac{p_{O_2}}{p^o}\right)^{1/2} \tag{16}$$

where ϕ_c and ϕ_e are the inner potentials of the cathode and electrolyte, $E_{N,c}$ and $\Delta\overline{G}_{cT}^{o}$ are the Nernst potential and molar Gibbs function change for reaction (2) at a temperature T and standard pressure p^o, and n_e is the number of electrons carried by an oxygen ion. Similarly, the potential difference across a point on the AEI is given by

$$\phi_e - \phi_a = E_{N,a} = -\frac{[\Delta\overline{G}_{aT}^{o}]}{n_e F} + \frac{\bar{R}T}{n_e F}\ln\left(\frac{p_{H_2}}{p_{H_2O}}\right) \tag{17}$$

where ϕ_a is the inner potential of the anode and $E_{N,a}$ and $\Delta\overline{G}_{aT}^{o}$ are the Nernst potential and molar Gibbs function change for reaction (3).

When the half-cell reactions (Eqs. (2) and (3)) depart from equilibrium, the current density that flows across either the CEI or AEI is found from the Butler–Volmer equation

$$i = i_0\left[\exp\left(\frac{\alpha n_e F \Delta E_A}{\bar{R}T}\right) - \exp\left(-\frac{(1-\alpha)n_e F \Delta E_A}{\bar{R}T}\right)\right] \tag{18}$$

where i_0 is the exchange current density, α is a charge transfer coefficient, and ΔE_A is the activation loss. ΔE_A is the calculated departure of each reaction from equilibrium and is given by

$$\Delta E_{A,c} = (\phi_c - \phi_e) - E_{N,c}, \quad \Delta E_{A,a} = (\phi_e - \phi_a) - E_{N,a} \tag{19}$$

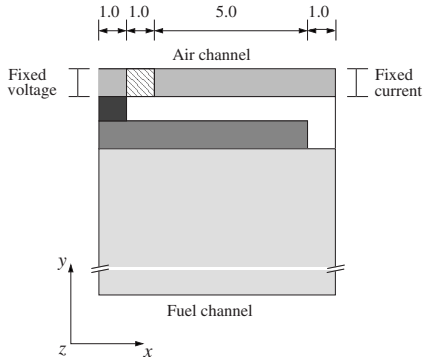

Fig. 5 Cross-section through the computational domain (all dimensions are in millimeters)

for the reactions at the CEI and AEI, respectively.

Many authors have proposed different models for i_0, and the work presented in this study is based on the models of Costamagna et al. [7] where $\alpha_c=\alpha_a=0.5$ and i_0 is given by

$$i_{0,c} = 7\times 10^8\left(\frac{p_{O_2}}{p^o}\right)^{1/4}\exp\left(-\frac{120\times 10^3}{\bar{R}T}\right) \tag{20}$$

$$i_{0,a} = 5.5\times 10^8\left(\frac{p_{H_2}}{p^o}\right)^{1/2}\left(\frac{p_{H_2O}}{p^o}\right)^{1/2}\exp\left(-\frac{100\times 10^3}{\bar{R}T}\right) \tag{21}$$

where the subscripts a and c denote the anode and cathode, respectively. The calculated current density is used to find the molar reaction rate for each half-cell reaction and hence the corresponding mass flux of each gaseous species at the CEI and AEI.

3 Physical Model

The computational domain for this study comprises just one fuel cell and the underlying porous support layer (see Fig. 5). Although this geometry is invariant in the z-direction, a three-dimensional computational domain is used with a uniform depth of 5 mm. Fixed voltage and fixed current density boundary conditions are prescribed on the cathode faces highlighted in Fig. 5 to simulate the net flow of current through the cell in the x-direction. Overall, the computational domain is very thin. Therefore isothermal operation is assumed, and a uniform operating temperature is prescribed (see Table 1). Fixed gas property boundary conditions are specified on the top faces of the cathode and the bottom face of the porous support layer to represent the air and fuel channels (see Table 1). These properties represent the typical operating conditions of a high temperature fuel cell such as the IP-SOFC, which is run on a fuel mixture obtained from the indirect reforming of natural gas. All the other external boundaries of the computational domain are specified as solid electrically insulating walls. The physical properties and thicknesses of each layer are given in

Table 1 Boundary conditions

Uniform operating condition	
$T=1138$ K	
Fuel channel	Air channel
$p=100$ kPa	$p=100$ kPa
$X_{H_2}=0.340$	$X_{O_2}=0.21$
$X_{H_2O}=0.330$	$X_{N_2}=0.79$
$X_{CO}=0.180$	
$X_{CO_2}=0.150$	

Table 2 Physical properties of the model components

Property		Porous support	Anode	Electrolyte	Cathode	Interconnect
Porosity	ε	0.20	0.20	0.00	0.20	0.00
Tortuosity	β	2.5	2.5	0	2.5	0
Pore diameter	d_p (μm)	2	1	0	1	0
Electric conductivity	σ_e (S mm^{-1})	—	33.3	—	50	0.02
Ionic conductivity	σ_i (S mm^{-1})	—	—	0.00735	—	—

Table 2. The notional gas conditions and material properties given in Tables 1 and 2 are for illustrative purposes only and do not represent any particular design.

4 Governing Equations

The governing equations are presented here in their time dependent form where time is a pseudovariable simply used to facilitate convergence to the steady-state solution. The conservation of each gas species in a porous material is described by

$$\varepsilon \frac{\partial \rho_{g,n}}{\partial t} = -\nabla \cdot \mathbf{G}_n \tag{22}$$

where the total mass flux of each gas species $\mathbf{G}_n$ can be found directly from the CPIM equations (see Eqs. (8) and (9)). The conservation of the electric or ionic charge within the current carrying layers is described by

$$\frac{\partial \rho_c}{\partial t} = -\nabla \cdot \mathbf{i} \tag{23}$$

where ρ_c is the charge density. It has been assumed that the cell operates isothermally. Hence it is not necessary to solve an energy conservation equation.

5 Numerical Scheme

The conservation equations are solved using an explicit time-marching finite volume method, which has been implemented in the new SOHAB computer code. The SOHAB code operates on a three-dimensional structured rectangular grid with variables stored at cell vertices (see Fig. 6). Thus a geometrically complicated computational domain, such as the one being considered in this study, is split into a series of rectangular grids that communicate through their boundary conditions. The numerical scheme is based on the methods published by Denton [17] and Haberman and Young [18–20]. It should be noted that this numerical method is not currently time accurate, and, as mentioned earlier, time is used as a pseudovariable to allow convergence to the steady-state solution.

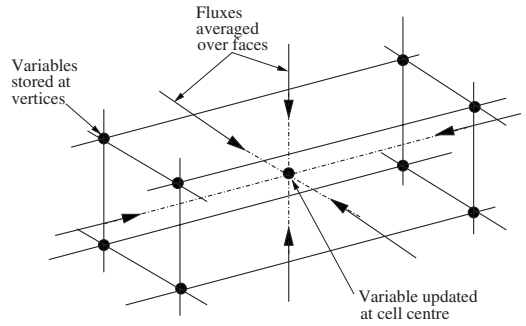

Fig. 6 Diagram showing a computational cell and the storage of information

6 Results

The results presented below were calculated using the boundary conditions and physical properties described in Sec. 3 and presented in Tables 1 and 2, which represent notional dimensions and operating conditions for a high temperature fuel cell such as the IP-SOFC.

6.1 Code Validation. Several tests were performed to validate the SOHAB code and to establish the mesh density required to produce accurate results in a reasonable CPU time. The implementation of the CPIM in the SOHAB code has been extensively validated against experiments on the counter flow of a binary gas mixture through a porous layer [14,16].

The SOHAB current flow model was validated against the analytical work of Costamagna et al. [7] and Bossel [8] who modeled the current flow path shown in Fig. 4 by neglecting the electrochemical reactions and assuming that current could flow freely between the electrolyte and electrodes. Using this model in conjunction with Ohm's law, the total resistance of the cell geometry (see Fig. 5) was calculated to be 0.797 Ω. Numerical simulations were performed that also neglected the electrochemical reactions, and results were obtained for a wide range of computational grids so that a mesh sensitivity study could also be performed (see Table 3). A comparison between the analytical and numerical results shows that an excellent agreement is obtained using a com-

Table 3 Calculated Ohmic resistance

Number of grid cells across		Calculated Ohmic resistance (Ω)
Electrolyte	Interconnect	
5	5	0.764
10	10	0.791
15	15	0.795
20	20	0.797
25	25	0.797

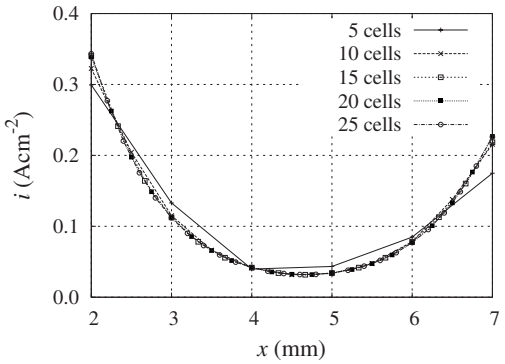

Fig. 7 The calculated current density *i* distribution along the width of the electrolyte obtained for different computational grid resolutions

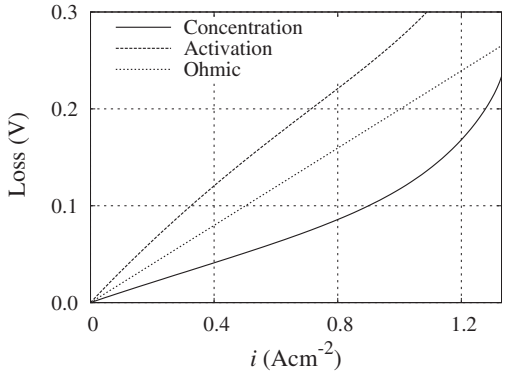

Fig. 8 The variation of each cell loss mechanism with applied current density, calculated separately

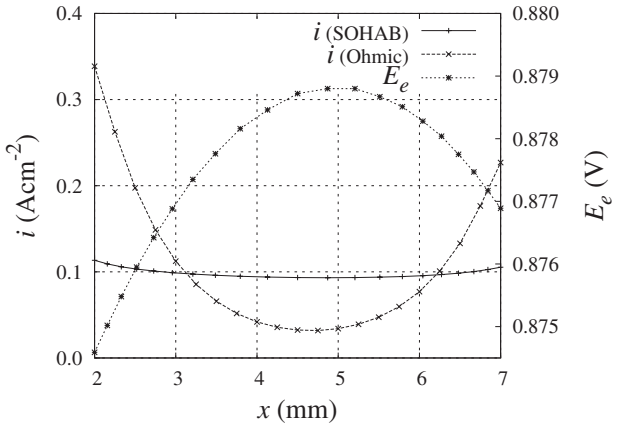

Fig. 10 A comparison between the current density distributions predicted by the SO-HAB code and a purely Ohmic model. The spatial variation of the potential difference across the electrolyte E_e is also shown.

putational grid representing the width of both the interconnect and electrolyte with 20 grid cells. Figure 7 shows a plot of the current density distribution along the width of the electrolyte calculated for each grid and confirms that a grid of 20 cells produces accurate results.

6.2 Test Cases. The current density distribution within the cell is controlled by the interaction between the activation, concentration, and Ohmic losses. Figure 8 shows a comparison between losses where each loss was evaluated separately using a one-dimensional model representing a line through the four layers of the fuel cell model. A uniform current density i was applied across the electrolyte, and the resulting gas conditions on its electrode interfaces were found. A comparison using Eq. (4) was made between these conditions and the fixed properties given in Table 1 to estimate the concentration loss. The activation losses for the anode and cathode were calculated using the kinetic models given in Sec. 2.3 and the electrolyte gas conditions predicted above. The Ohmic loss was estimated from the total resistance of the cell (see Sec. 6.1).

Figure 8 shows that the different losses are of similar magnitudes. The rate of increase in the activation loss is highest at low values of i, whereas the opposite is true for the concentration loss. The magnitudes of the losses suggest that the current density distribution of the cell is activation loss dominated. The relative size of the Ohmic loss steadily increases with the current drawn through the cell, suggesting that the current density distribution will become increasingly affected by the Ohmic behavior of the cell.

An initial test case was chosen to illustrate how the current density distribution within the electrolyte is controlled by the interplay between the three loss mechanisms. The computational grid identified from the convergence study and the fixed boundary conditions and material properties given in Sec. 3 were used. A fixed current was drawn through the cell that corresponded to a mean current density of $i_{mean}=0.1$ A cm^{-2} in the electrolyte.

Figure 9 shows a plot of conventional current density vectors in the x-y plane of the cell for this test case. The current flow path is typical for a segmented-in-series cell and is similar in appearance to that assumed in the purely Ohmic model of Bossel [8] (see Fig. 4). The conductivity of the electrolyte and interconnect are much lower than the electrodes, and as a result the current spreads preferentially throughout the high conductivity electrodes in the x-direction and appears to flow uniformly through the electrolyte in the y-direction.

On closer inspection, it is possible to see that the current density distribution is not uniform (see Fig. 10). The current density is highest at $x=2$ mm as the current preferentially flows from the anode into the lower resistance cathode. Figure 10 also shows a comparison to the current density predicted by a purely Ohmic model, as used in Sec. 6.1. This Ohmic model predicts very high current densities at the edges of the electrolyte, whereas the SO-HAB code, which includes models for the activation and concentration losses, predicts a much more uniform current density distribution. These two losses reduce the potential difference produced across the electrolyte E_e, especially in regions of locally high current density, which leads to a much more uniform distribution. Figure 10 also plots the variation of E_e and shows that as expected it is smallest near the edges of the electrolyte where the

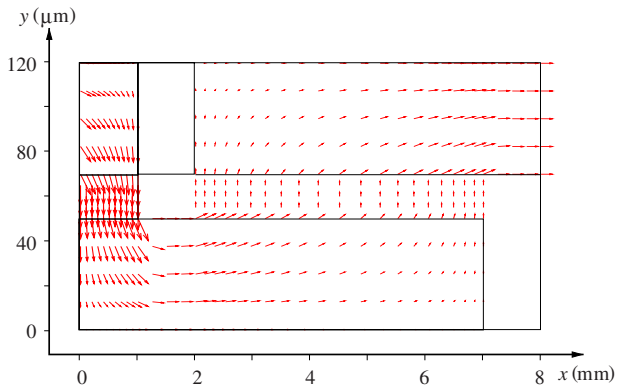

Fig. 9 Vectors of conventional current density plotted in the *x-y* plane of the cell

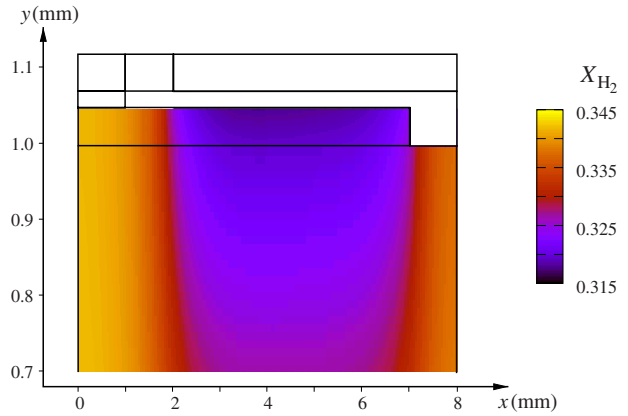

Fig. 11 Hydrogen mole fraction X_{H_2} distribution plotted in the *x-y* plane of the cell

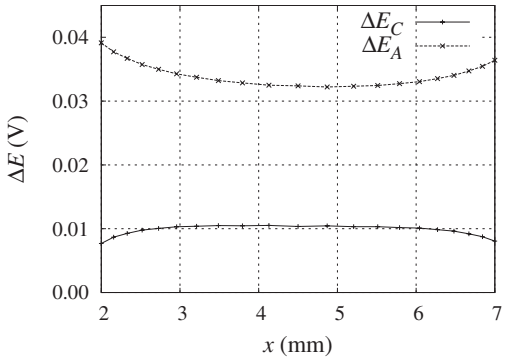

Fig. 12 The spatial variation of concentration ΔE_C and activation ΔE_A losses along the width of the electrolyte

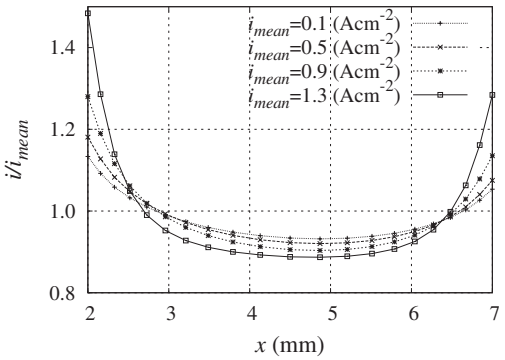

Fig. 14 Comparison between the normalized current density distributions obtained at different mean electrolyte current densities

current density is highest.

Figure 11 shows a plot of the hydrogen mole fraction X_{H_2} distribution in the x-y plane of the cell. X_{H_2} is lowest at the AEI where hydrogen is consumed by the electrochemical reaction, and it diffuses toward this region from the surrounding fuel side parts of the cell. H_2 can also diffuse to the edges of the electrolyte in the x-direction from the surrounding inactive regions of the cell, and the lowest value of X_{H_2} is found in the center of the AEI where the electrolyte current density is at a minimum. A similar plot is obtained for the distribution of the steam mole fraction X_{H_2O} except that it increases at the AEI where it is produced by the electrochemical reaction. There is much less X_{O_2} variation in the cathode than in the fuel gases mentioned above because it is very thin and constrained by the electrolyte on one side and by the prescribed boundary conditions on the other.

The results presented above suggest that the concentration loss ΔE_C is not responsible for flattening the current density distribution and that this effect occurs primarily as a result of the activation loss ΔE_A. This is confirmed in Fig. 12, which shows the spatial variation of the two losses. The activation loss is larger than the concentration loss and is largest near the edges of the electrolyte where the current density is highest. The concentration loss shows very little variation and is smallest near the edges of the electrolyte because of gases diffusing in the x-direction, as shown in Fig. 11

Several further test cases were run to establish how the current density distribution is affected by the mean current density i_{mean} drawn through the electrolyte. Figure 13 shows a comparison between the distributions obtained at different values of i_{mean}. The shape of the distributions becomes more peaked at their edges as i_{mean} is increased, and the Ohmic behavior of the cell becomes more visible. This observation is confirmed in Fig. 14, which shows current density distributions that have been normalized by i_{mean} to allow a better comparison between them. At very high values of i_{mean}, the effects of the concentration loss become visible and the middle of the current density distribution becomes more flattened. This flattening does not extend to the edges of the electrolyte due to the diffusion of gases in the x-direction mentioned above, and the distribution in these regions has become even more peaked.

Figure 15 shows the variation in the calculated output voltage of the cell with i_{mean}. For comparative purposes, the results obtained by summing the individual losses shown in Fig. 8 where a uniform current density distribution was assumed are also plotted. There is a good agreement at low values of i_{mean}, which suggests that current density distribution calculated by the SOHAB code is sufficiently flat to allow a uniform current density approximation to be made. However, there is an increasing error at large values of i_{mean} where this approximation tends to underestimate the output voltage. The main reason for this is that the concentration loss is smaller than expected as gases diffuse between the edges of the electrolyte and the inactive regions of the cell in the x-direction.

7 Conclusions

A new computer code known as the SOHAB code has been developed for investigating the behavior of SOFCs. In this study, the SOHAB code has been used to simulate the current flow within a segmented-in-series cell including the spatial variation of activation and concentration losses that result from the kinetics of the electrochemical reactions and the mass flow within the cell, respectively.

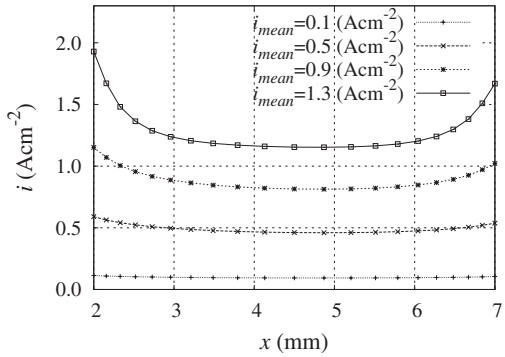

Fig. 13 Comparison between the current density distributions obtained at different mean electrolyte current densities

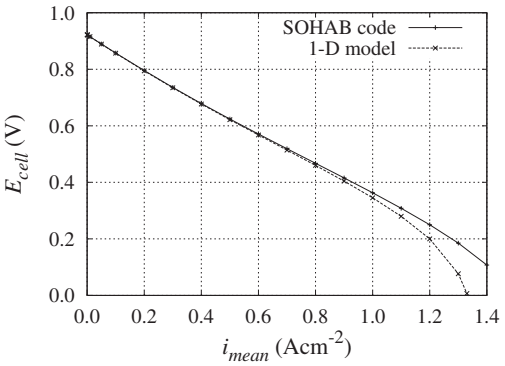

Fig. 15 The variation in calculated cell output voltage with mean current density drawn through the electrolyte i_{mean}. A comparison is also made to the result obtained using the one-dimensional (1D) model described in Sec. 6.2.

Several simulations were performed to fully understand the cell behavior, and comparisons were made to an analytical solution that considered the Ohmic behavior of the cell only. It was found that the purely Ohmic model predicted a very peaked current density distribution with high currents flowing near the edges of the electrolyte. However the SOHAB code, which included all the cell irreversibilities, predicted a much flatter distribution. This difference is caused by the strong coupling between the current density distribution and the spatial variation of the cell irreversibilities.

It was also found that the characteristics of the calculated current density distribution vary with the current drawn through the cell. At low currents the cell behavior is dominated by the activation loss and the current density distribution is almost uniform. As the current drawn is increased, the Ohmic behavior of the cell becomes apparent and the distribution becomes more peaked near the electrolyte edges but not to the extent predicted by the purely Ohmic models. At very high currents the effect of the increased concentration losses is visible as a further flattening of the central part of the distribution. However, this effect does not extend to the edges of the electrolyte where the concentration losses remain small because of the improved gas flow from the surrounding inactive areas of the cell.

Finally, a comparison was made over a range of applied currents between the cell output voltage predicted by the SOHAB code and the results from a simplified uniform current density model. A good agreement was obtained at low and moderate currents, suggesting that a uniform current density distribution is a valid assumption. However, at high currents this simplified model overestimates the concentration loss because it does not account for the improved gas flow near the electrolyte edges.

Acknowledgment

B.A.H. was supported by a Rolls-Royce Fuel Cell Systems Ltd. research grant, and the authors are grateful for the technical assistance supplied by their staff, particularly Dr. G. Agnew, Dr. R. Travis, and R. Collins.

Nomenclature

D_{nm} = binary diffusion coefficient
$D_{k,n}$ = Knudsen coefficient
d_p = mean pore diameter
$\mathbf{G}$ = total mass flux vector
$\mathbf{i}$ = current density vector
M = molar mass
N = number of species
p = pressure
R = specific gas constant
t = time
T = temperature
X = mole fraction
Y = mass fraction

Greek Letters

β = tortuosity
ε = porosity
ϕ = electric field potential
μ = dynamic viscosity
ρ = density
σ = electric or ionic conductivity

Subscripts

a = anode
c = cathode
e = electrolyte
g = gas
m = component species m
n = component species n
s = solid

Superscripts

d = diffusion

References

[1] Matsuzaki, Y., and Yasuda, I., 2008, "Electrochemical Oxidation of H_2 and CO in a $H_2-H_2O-CO-CO_2$ System at the Interface of a Ni-YSZ Cermet Electrode and YSZ Electrolyte," J. Electrochem. Soc., **147**, pp. 1630–1635.
[2] Singhal, S. C., and Kendall, K., eds., 2003, *High Temperature Solid Oxide Fuel Cells: Fundamentals, Design and Applications*, Elsevier, New York.
[3] Gardner, F. J., Day, M. J., Brandon, N. P., Pashley, M. N., and Cassidy, M., 2000, "SOFC Technology Development at Rolls-Royce," J. Power Sources, **86**, pp. 122–129.
[4] Singhal, S. C., 2000, "Advances in Solid Oxide Fuel Cell Technology," Solid State Ionics **135**, pp. 305–313.
[5] Nakamura, K., Yamashita, S., Tsutomu, S., and Seyama, T., 2005, "Development of SOFC Power Generation System Using Segmented-in-Series Cell Stacks Operating at Low Temperatures," *Proceedings of the First European Fuel Cell Technology and Applications Conference*, ASME, New York, p. 41.
[6] Pillai, M. R., Gostovic, D., Kim, H., and Barnett, S. A., 2007, "Short-Period Segmented-in-Series Solid Oxide Fuel Cells on Flattened Tube Supports," J. Power Sources, **163**, pp. 960–965.
[7] Costamagna, P., Selimovic, A., Del Borghi, M., and Agnew, G., 2004, "Electrochemical Model of the Integrated Planar Solid Oxide Fuel Cell (IP-SOFC)," Chem. Eng. J., **102**, pp. 61–69.
[8] Bossel, U. G., 1992, "Facts and Figures, Final Report on SOFC Data," International Energy Agency, Technical Report.
[9] Lai, T. S., and Barnett, S. A., 2005, "Design Considerations for Segmented-in-Series Fuel Cells," J. Power Sources, **147**, pp. 85–94.
[10] Ferguson, J. R., Fiard, J. M., and Herbin, R., 1996, "Three-Dimensional Numerical Simulation for Various Geometries of Solid Oxide Fuel Cells," J. Power Sources, **58**, pp. 109–122.
[11] Iwata, H., Hikosaka, T., Morita, M., Iwanari, T., Ito, K., Onda, K., Esaki, Y., Sakaki, Y., and Nagata, S., 2008, "Performance Analysis of Planar-Type Unit SOFC Considering Current and Temperature Distributions," Solid State Ionics, **132**, pp. 297–308.
[12] Yakabe, H., and Sakurai, T., 2004, "3D Simulation on the Current Path in Planar SOFCs," Solid State Ionics, **174**, pp. 295–302.
[13] Manadin, P., Bernay, C., Tran-Dac, S., Broto, A., Abes, D., and Casssir, M., 2006, "SOFC Modelling and Numerical Simulation of Performances," Fuel Cells, **6**, pp. 71–78.
[14] Haberman, B. A., and Young, J. B., 2008, "A Detailed Three-Dimensional Simulation of an IP-SOFC Stack," ASME J. Fuel Cell Sci. Technol., **5**(1), p. 011006.
[15] Young, J. B., and Todd, B., 2005, "Modelling of Multi-Component Gas Flows in Capillaries and Porous Solids," Int. J. Heat Mass Transfer, **48**, pp. 5338–5353.
[16] Haberman, B. A., and Young, J. B., 2006, "Diffusion and Chemical Reaction in the Porous Structures of Solid Oxide Fuel Cells," ASME J. Fuel Cell Sci. Technol., **3**, pp. 312–321.
[17] Denton, J. D., 1992, "The Calculation of Three-Dimensional Viscous Flow Through Multistage Turbomachines," ASME J. Turbomach., **114**, pp. 18–26.
[18] Haberman, B. A., and Young, J. B., 2005, "Numerical Investigation of the Air Flow Through a Bundle of IP-SOFC Modules," Int. J. Heat Mass Transfer, **48**, pp. 5475–5487.
[19] Haberman, B. A., and Young, J. B., 2004, "Three-Dimensional Simulation of Chemically Reacting Gas Flows in the Porous Support Structure of an Integrated-Planar Solid Oxide Fuel Cell," Int. J. Heat Mass Transfer, **47**, pp. 3617–3629.
[20] Haberman, B. A., 2005, "Three-Dimensional Simulation of the Integrated-Planar Solid Oxide Fuel Cell," Ph.D. thesis, University of Cambridge, Cambridge, UK.